PAPER

Check for updates

Enhanced polarization and dielectricity in BaTiO₃:NiO nanocomposite films modulated by the microstructure†

M. J. Chen, X. K. Ning, [ID]* S. F. Wang* and G. S. Fu

Parallel and vertical interfaces in vertically and parallelly aligned nanocomposite thin films have been shown to be an effective method to manipulate functionalities. However, tuning the physical properties by modulating the microstructure of the self-assembled nanocomposite films and understanding the physical properties underlying the manipulation is still a challenge. In this work, BaTiO₃:NiO (BTO:NiO) nanocomposite films with nanomultilayer, nanocolumnar and nanogranular structures have been prepared on Nb:SrTiO₃ (Nb:STO) substrates by a pulsed laser deposition (PLD) method. These films have been used as a model system to investigate the relationship between the microstructure and the ferroelectric properties. The polarization, dielectricity and leakage can be separately modulated by tuning the microstructures. The experimental results show that the remanent polarization of the nanocomposite films is much higher than that of the pure BTO films. By precisely modulating the microstructure, a significantly enhanced polarization (>70% higher than pure BTO for the nanomultilayer structure) and dielectricity (>60% and >240% higher than pure BTO for the nanomultilayer and nanocolumnar structure, respectively) are realized in these films. These results demonstrate that tunable ferroelectric properties can be realized by controlling the microstructures in the epitaxial BTO:NiO nanocomposite thin films, which will be expected to be applied in the devices such as supercapacitors, solar cells and non-volatile memory applications.

Introduction

Artificially layered and self-assembled nanocomposites, in which two phases grow epitaxially with each other, provide many opportunities to develop systems with novel and enhanced functionalities.[1,2] These materials have shown tremendous potential in technological applications in recent years because of their potential application in next-generation technological devices, for instance, non-volatile random access memories (RAM),[3] tunnel junctions,[4] and photocatalysis as well as energy conversion.[5,6] The properties of these nanostructures depend significantly on nanostructure morphology as well as orientation.[7–9] Especially, functional properties of these nanocomposite films, such as low-field magnetoresistance (LFMR),[10,11] magnetoelectric properties,[12,13] electronic-transport properties,[14,15] ferroelectric (FE) properties[16,17] and dielectric properties[18] tremendously depend on the size, shape, and arrangement of each constituted phase in these composite films. Therefore, manipulation of the micro-structures of

nanocomposite films can be expected to give rise to rich tunable functionalities.

As far as FE nanocomposites are concerned, due to the possibilities for applications that include supercapacitors as well as the increased storage densities for the FE random storage,[19,20] the perovskite FE oxides (*e.g.*, Pb(ZrTi)O₃, BaTiO₃, and BiFeO₃) have to date been the most popular materials to synthesis of nanocomposite films with highly controllable microstructure. Recently, remarkable improvement in oxide thin-film techniques have allowed for the growth and characterization of FE heterostructures with (near) atomic precision, opening an avenue for the fabrication of the nanocomposite films with different microstructures. The highly ordered nanocomposite FE films show enhanced polarization and dielectric properties, leading to the rapidly development of the research in the field of FE-RAM devices.

Up to now, due to the deepening cognition of the intrinsic and extrinsic polarization, dielectric and FE nanodomain, growing attention has been paid to BaTiO₃ (BTO) FE nanocomposite films. In these nanocomposite films, microstructures with nanogranular, nanomultilayer and nanocolumnar characteristics according to the distribution and arrangement of the second phase have been well studied. For example, firstly, artificial BTO nanocomposites films with the nanomultilayer configuration have drawn considerable attention due to

Hebei Key Lab of Optic-electronic Information and Materials, The College of Physical Science and Technology, Hebei University, 180 Wusi Road, Baoding 071000, China. E-mail: xkning@alum.imr.ac.cn; sfwang@hbu.edu.cn

a remarkable enhancement in polarization and resistivity. Unusual ferroelectricity in this structure is expected to be used in the preparation of high-performance microelectronic devices.[21,22] In 1994, Tabata *et al.* have firstly synthetized BTO/SrTiO$_3$ (BTO/STO) nanocomposites films with nanomultilayer structure by Pusled Laser Deposition (PLD), in which BTO and STO formed layered structure and epitaxially grown with each other.[23] Lee *et al.* fabricated a series of CaTiO$_3$/BTO/STO superlattices, and found an enhancement in the FE properties with respect to pure BTO films.[24] In charge- or orbital-mediated artificial layered structure of the BTO/Pb(Zr$_{0.52}$Ti$_{0.48}$)O$_3$ (BTO/PZT) and BTO/LaNiO$_3$, the interfacial charge carrier density modulated by polarization charge determined the functional properties. For the nanomultilayer structure, the polarization properties could be improved as compared with the pure films, due to the preserving full strain and combining hetero-interfacial couplings.[23–26] In addition, oxygen vacancy accumulation as well as the charge transfer at the interface for the nanomultilayer structure also plays an important role in inducing the local polarization enhancement.[27] Secondly, BTO based naonocomposite thin films with nanogranular configuration also produced a tremendous flurry of research interest because of their unique physical and chemical properties. Ge *et al.* have shown that the Co and Ni nanocrystals in the face-center cubic structure dispersed well in the single BTO matrix.[28,29] Their results provide an effective way to engineer BTO/Ni or BTO/Co nanocomposite films with desired qualities. Metal-BTO nanocomposite films, such as BTO/Ag, BTO/Co and PbTiO$_3$/Pb (PTO/Pb) composite films, have showed enhanced optical and electrical properties.[30–32] For the nanogranular structure, the embedded nanoparticles lead to the coarsening and coalescence of crystal grains of the FE films and improve the polarization properties for the nanogranular structure.[28,30] The permittivity and tunability in this structure also been tuned by conductive nanoparticles as the field-induced permittivity was estimated for different volume fraction of conductive particles.[30,33] Thirdly, BTO based naonocomposite thin films with nanocolumnar structure have also been studied extensively as the enhanced dielectric properties. Vertical interfaces in vertically aligned nanocomposite thin films have been approved to be an effective method to manipulate functionalities. Zheng *et al.* have studied the BTO:CoFe$_2$O$_4$ (BTO/CFO) nanocomposite films with the nanocolumnar structure to explore the ferroelectromagnets. Thermodynamic analyses show that the magnetoelectric coupling in such a nanostructure can be understood on the basis of the strong elastic interactions between the two phases.[34] Lee *et al.* have created a nanoscaffold Ba$_{0.6}$Sr$_{0.4}$TiO$_3$:Sm$_2$O$_3$ (BSTO:SmO) composite films with nanocolumnar structure which have a very high tunability which scales inversely with loss.[35] In addition, (BTO)$_{1-x}$:(SmO)$_x$ thin films with nanocolumnar configuration show a dielectric relaxation behavior due to the sinks to attract oxygen vacancies at the vertical interfaces.[18] For the nanocolumnar structure, the large vertical strain and strong elastic interactions could lead to the enhancement for the polarization and permittivity.[34,35]

However, on the one hand, the reported enhancement of dielectric for BTO based naocompsoites films with nanomultilayer structure is still too slight compared with the pure films. For the nanogranular structure, most of these studies have just focused on the dielectric or optical properties of these nanocomposite thin films, very little has been done to understand the polarization properties as they are too conducting for application of macroscopic electric fields. What's more, very weak polarization properties have been measured for the nanocolumnar structure which hinder the application for polarization-controllable functional devices. On the other hand, the microstructure plays the key role in determining the electrical properties for the BTO based nanocomposite films. Experimental studies on controlling the microstructure of the composite films are usually carried out by changing the volume fraction of the second phase. However, interestingly, extreme enhancement of the functionalities always appears in the vicinity of one critical content of the second phase which correlates with the transformation of the microstructures.[7,10,36] Therefore, the tuning of the microstructures of the nanocomposite films at a critical content of the second phase could help us to tailor their desirable functionalities.

In this study, the NiO, which is economical, eco-friendly, stability, lattice-matching with BTO and owns unique properties at nanometer sizes, has been used to prepare BTO nanocomposite thin films by PLD method. Of the transition-metal monoxides, NiO has received by far the greatest amount of attention, prompted by a remarkable range of motivations.[37] The values of the dielectric constant of NiO have a weak temperature dependence which is important for the stability of the device.[38] It is noted that NiO has been one of the most promising candidates because it has a high melting point and exhibits the highest increase in the dielectric constant compared to other metal monoxides for the BTO FE materials.[39,40] What's more, as compared to their corresponding counterparts epitaxially grown on the substrates, the type of the perovskite titanate and structure is one of the most important issues to modulated the FE properties.[41] In the bulk composites, the addition of NiO was more effective in broadening dielectric constant peaks and values.[42,43] For the BTO:NiO composties, the switching polarities for the two semiconductors are opposite to each other and the interdiffusion between the BTO grains and NiO can affect the rather complex dielectric dispersion and conductivity spectra.[44,45] Hence, the enhanced polarization and dielectric constant may be realized by controlling the geometry structures of NiO with BTO in the BTO:NiO nanocomposite thin films. The experimental results show that the remanent polarization, leakage and dielectric constant, can be well modulated by tuning the NiO fraction and the microstructure.

Experimental

Synthesis of the films

BTO:NiO nanocomposite thin films with a thickness of 120–180 nm were grown on Nb-doped SrTiO$_3$ single-crystal (Nb:SrTiO$_3$ with 0.7 wt% of Nb, abbreviated as Nb:STO) (001) substrates by PLD using a XeCl ($\lambda = 308$ nm) excimer laser. The laser flux is approximately 1.2 J cm^{-2} with a repetition rate of 2 Hz. BTO and NiO thin films were deposited on Nb:STO

substrates at 0.2 mbar pressure of pure O_2 at a substrate temperature of 630 °C. The distance between the target and the substrate was 35 mm. Prior to deposition, the substrates were ultrasonically cleaned with acetone followed by ethanol. The chamber was evacuated using a turbo-pump down to about 2 do10^{-5} Pa to remove any extraneous particles. The samples were finally annealed at a pressure of 0.5 bar of pure O_2 to remove oxygen vacancies (deposition parameters and their levels see Table S1†). For fabricating the composite films with different geometry microstructures with the same NiO ratios, the composite $(BTO)_{0.9}:(NiO)_{0.1}$ and $(BTO)_{0.8}:(NiO)_{0.2}$ targets and two single BTO and NiO targets have been used. The $(BTO)_{0.9}:(NiO)_{0.1}$ and $(BTO)_{0.8}:(NiO)_{0.2}$ ceramic target were made by BTO, and NiO powders (99.99%) in proper ratios and following multiple steps of standard solid state reaction processes. The single BTO and NiO targets are directly synthetized by BTO and NiO powder (99.99%), respectively (targets parameters and their synthetized materials see Table S2†). In this paper, to produce the BTO:NiO nanocomposite films with the nanomultilayer and nanocolumnar structures, two separated targets of BTO and NiO were alternately used to deposit BTO and NiO on the Nb:STO substrate, as shown in Fig. 1(a) and (b). The preparation process can be expressed as a formula of $[(BTO)t_1/(NiO)t_2]n$, where, t_1 and t_2 are the deposition times for BTO and NiO, respectively, and n is their repeat number. These three important parameters, t_1, t_2, and n, were used to control the composition, thickness, and microstructure of the BTO:NiO nanocomposite films. First, we tune the microstructure for the NiO volume fractions of 10%, 20%, and 30%, where the deposition times were taken as $t_1 = 8$–30 and $t_2 = 100$ s, respectively, and the growth shows Frank–van der Merwe, or layer-by-layer growth behavior.[46] When the seed layers of the BTO and NiO phases expand in two dimensions, a planar layer of the BTO and NiO phases will form, as shown in Fig. 1(a). The samples will hereafter be denoted as M-1, M-2 and M-3 with the NiO ratio about 10, 20% and 30% for the nanomultilayer configuration, respectively. The parameters for each sample are summarized in Table 1. To obtain a nanocolumnar microstructure, the deposition times for BTO and NiO are $t_1 = 1$–3 s and $t_2 = 10$ s. The targets have to be rotated sufficiently fast to ensure that BTO or NiO seed nuclei were not attached with each other to initiate an island-type growth mode (Volmer–Weber model) at an early stage, as shown in Fig. 1(b). The samples will hereafter be denoted as C-1, and C-2 with the NiO ratio about 10% and 20% for the nanocolumnar configuration, respectively. In our previous study,[7] under this island-type growth mode, the deposited particles of BTO and NiO more strongly bond to their own phase and coherently build up the columnar configuration, as shown in Fig. 1(b). This is energetically favorable for the growth because the lattice mismatch and strain are decreased, giving rise to the formation of a nanocolumnar microstructure.[7] For nanocomposite films with a nanogranular structure (the samples will be denoted as G-1 and G-2) have been deposited by using a single composite $(BTO)_{0.9}:(NiO)_{0.1}$ and $(BTO)_{0.8}:(NiO)_{0.2}$ target, as shown in Fig. 1(c).
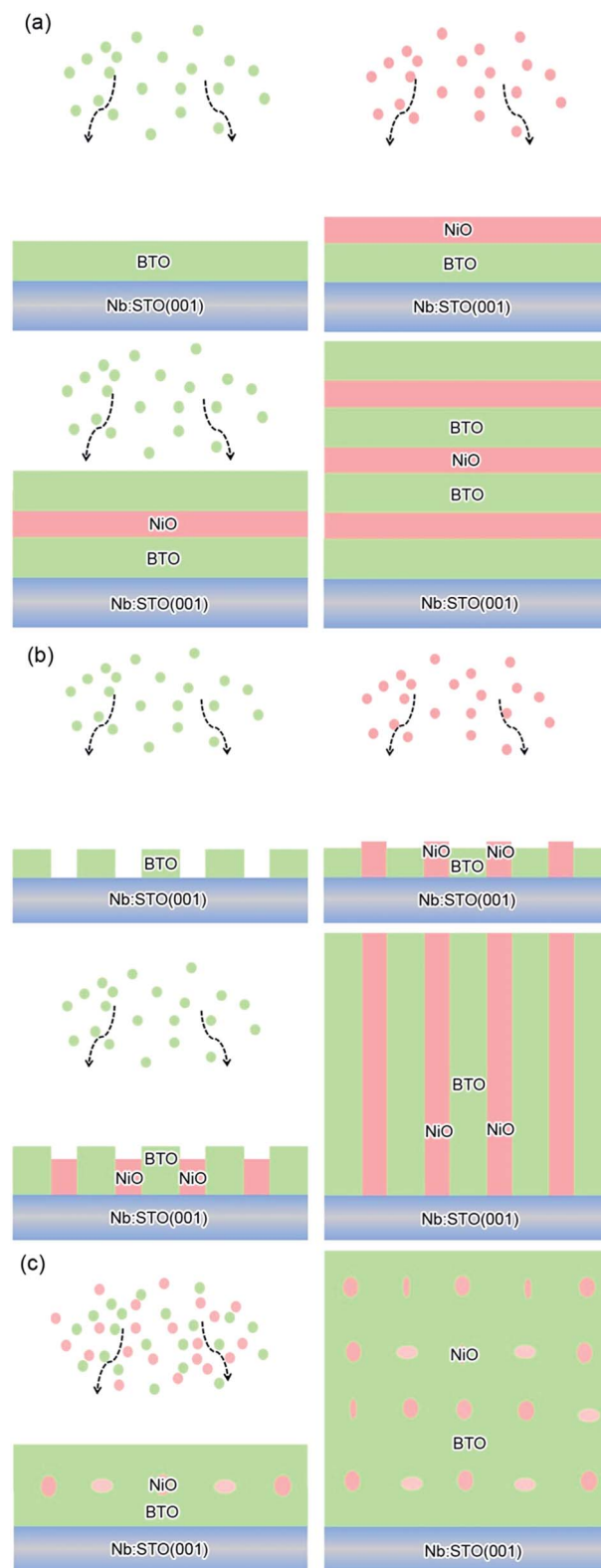

Fig. 1 Schematic illustrations of the growth modes for the BTO:NiO nanocomposite films with equal volume fractions of BTO and NiO but with different microstructures: (a) nanocolumnar nanomultilayer configuration, (b) configuration and (c) nanogranular configuration.

Table 1 Deposition parameters and their levels

Label	Samples	Target	t_1 (s)	t_2 (s)	n	d (nm)
M-1	$(BTO)_{0.9}:(NiO)_{0.1}$	BTO and NiO	8	100	35	160
M-2	$(BTO)_{0.8}:(NiO)_{0.2}$	BTO and NiO	13	100	30	145
M-3	$(BTO)_{0.7}:(NiO)_{0.3}$	BTO and NiO	30	100	28	140
C-1	$(BTO)_{0.9}:(NiO)_{0.1}$	BTO and NiO	1.5	10	200	130
C-2	$(BTO)_{0.8}:(NiO)_{0.2}$	BTO and NiO	3	10	200	125
G-1	$(BTO)_{0.9}:(NiO)_{0.1}$	$(BTO)_{0.9}:(NiO)_{0.1}$	—	—	—	130
G-2	$(BTO)_{0.8}:(NiO)_{0.2}$	$(BTO)_{0.8}:(NiO)_{0.2}$	—	—	—	140

Apparatus

The crystal structure and orientation of the BTO:NiO films were analyzed by θ–2θ scans of X-ray diffraction (XRD, Rigaku RINT2000, Cu K_α radiation). Transmission electron microscopy (TEM) specimens for both cross-sectional and plan view observations were prepared by conventional method, *i.e.*, by the standard procedure of cutting, gluing, slicing, grinding and finally ion milling with Ar$^+$ ions until they were electron transparent. A Gatan precision ion polishing system (PIPS 695; Gatan) with a liquid–nitrogen-cooled stage was used to prevent the cross-sectional specimens from preferential thinning effects. Plan view specimens were milled only from the substrate side. The microstructures of the films were characterized by TEM (Tecnai G2 F20, accelerating voltage 200 kV). A Tecnai G2 F30 transmission electron microscope, equipped with a high-angle-annular-dark-field (HAADF) detector and a post-column Gatan (Titan Cubed 60–300 kV microscope (FEI) fitted with a high-brightness field emission gun (X-FEG) and double Cs correctors from CEOS, and a monochromator operating at 300 kV), was used for Z-contrast imaging analysis. The FE properties of the films were measured by using a standard FE testing system (TF2000E; Aixacct). The dielectric constant and loss were measured in a frequency range of 1–100 kHz using an impedance analyzer LCR Hitester (HIOKI 3532-50). The chemical valence of the ions in the BTO:NiO films were determined by X-ray photoelectron spectroscopy (XPS, Therma ESCALAB 250; Al $K\alpha$ source, 1486.60 eV, resolution: 400 meV, energy step: 0.1 eV).

Results and discussion

Fig. 2(a) shows XRD patterns of the $(BTO)_{1-x}:(NiO)_x$ nanomultilayer films with different NiO ratios (x = 0.1, 0.2 and 0.3, abbreviated as M-1, M-2 and M-3, respectively). In all the samples, diffraction peaks of the BTO and NiO phases around the diffraction peaks of (002) planes for the Nb:STO substrate are observed, indicating that the BTO and NiO layers grown epitaxially on the Nb:STO (001) substrate. The epitaxial nature of the films is also confirmed by the TEM results presented later. Fig. 2(b) illustrates that, with increasing NiO content, the (002) reflection of BTO and the (200) reflection of NiO shift to higher angles. Based on these diffraction peaks, we can calculate the out-of-plane lattice parameters of the BTO and NiO layers in the nanomultilayer. The corresponding decrease of the lattice parameters of the BTO and NiO phases with increasing NiO fraction is depicted in Fig. 2(d). The BTO, epitaxially grown on the
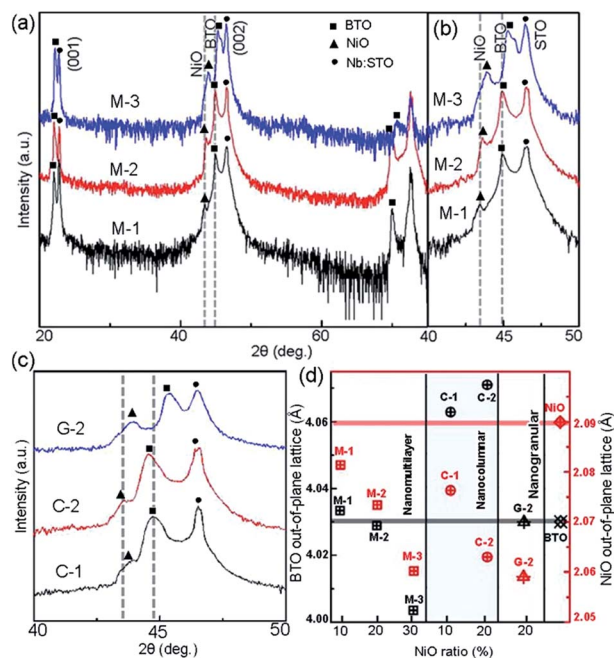

Fig. 2 (a and b) XRD patterns of the BTO:NiO nanomultilayer with different NiO contents (left) and an enlarged XRD scan around the (002) diffractions of the samples. (c) Lattice parameters of the BTO and NiO as a function of the NiO fraction and microstructure. (d) The corresponding decrease of the lattice parameters of the BTO and NiO phases with increasing NiO fraction.

Nb:STO substrate, will experience in-plane compressive stress due to the lattice mismatch between BTO (a = 4.015 Å) and Nb:STO (a = 3.91 Å). Because of the presence of NiO (a = 4.172 Å), the BTO will experience tensile stress arising from the clamping constraints of the NiO. Conversely, the NiO will experience in-plane compressive stress arising from the clamping constraints of the BTO. Therefore, the lattice parameters of BTO decrease with increasing NiO content. Fig. 2(c) shows XRD patterns of the $(BTO)_{1-y}:(NiO)_y$ nanocolumnar films and nanogranular films with different NiO concentration (y = 0.1, 0.2, abbreviated as C-1 and C-2 for the nanocolumnar films, respectively). G-2 is the nanogranular films with the NiO ratio about 20%. For the nanocolumnar films, as shown in Fig. 2(c), the (002) reflection of BTO and the (200) reflection of NiO shift to lower angles with increasing NiO content. The corresponding increase of the lattice parameters of the BTO phases with increasing NiO fraction is depicted in Fig. 2(d). Compared with the bulk value of BTO (a = 4.015 Å) and cubic NiO (a = 4.172 Å), the BTO and NiO is almost relaxed for the nanogranular composite films. It is noted that because of the presence of the vertical interfaces in the nanocolumnar films, the BTO will experience tensile stress arising from the clamping constraints of the surrounding NiO along the out-of-plane direction. Conversely, the NiO will experience out-of-plane compressive stress arising from the clamping constraints of the surrounding BTO. Therefore, the lattice parameters of BTO increase compared with the pure films.

TEM study has been conducted to characterize the microstructures and the epitaxial nature of the composite films. The films prepared with the growth mode of Fig. 1(a) have formed

nanomultilayer structures. Fig. 3(a) shows low-magnification TEM images for the M-2. The total thickness is about 145 nm, and the individual thickness for BTO and NiO layers is about 0.8 nm and 2 nm, respectively. It is clearly exhibited that the interface between the film and substrate in the samples is flat and sharp. NiO and BTO are two-phase separation forming a nanomultilayer structures along the out-of-plane direction. The HAADF micrograph in Fig. 3(b) reveals that the nano-multilayer exhibits perfect epitaxy. The sharp Z contrast across the interface indicates minimal interdiffusion at the interface, absence of any extended structural defects such as misfit dislocations or antiphase boundaries. Fig. 4 shows a vertical-view TEM images of the as-grown BTO:NiO films of the C-1 samples. The dotted line is the interfaces between the composite films and the Nb:STO substrates. At the composition of 0.1 for the NiO, a vertical columns at both the bottom and the top have been found. Fig. 4(b) and (c) show the high-resolution image of the NiO nanopillar (2–5 nm) within the BTO matrix. The spacing between them is about 5–10 nm. The typical HAADF micrographs of BTO–NiO columns have been conducted at the bottom and inner part of the C-1 sample, respectively. Fig. 4(b) and (c) demonstrate that the NiO nanopillar has very high epitaxial quality of these two phases and atomically sharp heterointerface between them. Also, STEM-EDX analysis (red dashed line in Fig. 4(b)) result confirms the alternating phase arrangement for the NiO in the BTO matrix (Fig. 4(d)). It can be observed that the NiO and BTO are separating into two phases

Fig. 4 (a) A cross-sectional TEM image of the nanocolumnar film C-1. (b) and (c) HRTEM displaying the nanopillar NiO at the bottom and inner part of the films. The dotted line is the interfaces between the composite films and the Nb:STO substrates. (d) STEM-EDX line scans the region of red dashed line in (b).
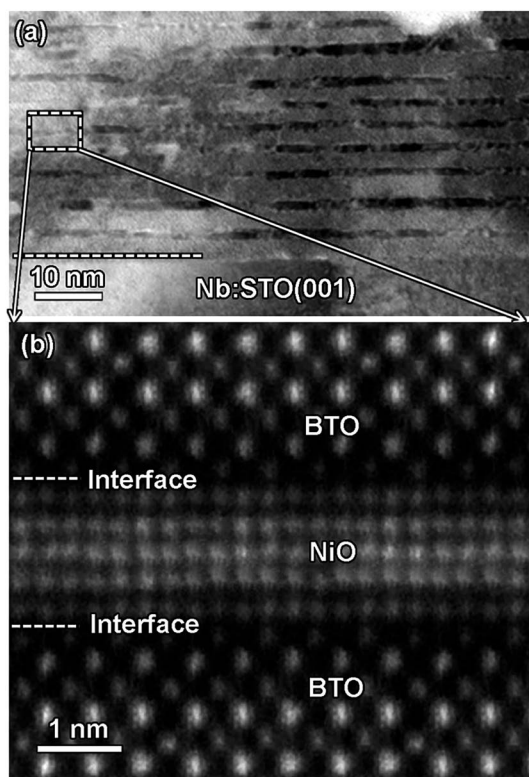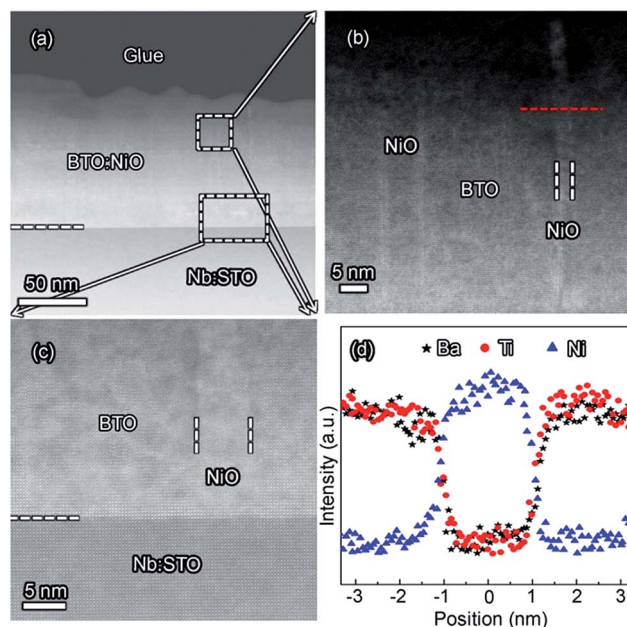

Fig. 3 (a) A cross-sectional TEM image of the nanomultilayer film M-2. (b) The high-angle annular dark-field (HAADF) micrograph of the film for the M-2.

and forming a columnar structure along the out-of-plane direction (indicated by the white dashed lines). This is because the radius of a Ni^{2+} ion (0.69 Å) is larger than that of Ti^{4+} ion (0.60 Å), and the larger Ni^{2+} ion enters into the lattice of BTO with difficulty and probably is being pushed out toward the phase boundary to release the local strain.[47] It is noted that the self-assembled nanocolumnar structures formed for the C-1 samples, from their low magnification TEM image and the high-resolution TEM (HRTEM) image. However, for the C-2, as shown in Fig. S1,† some planar structure is found at the base of the film. In addition, the diameter of the nanocolumnar increased (~5–10 nm) and the nanocolumnar become not so ordered compared with that in the C-1 samples (Fig. S1(b) and (d)†). To better understand the microstructures of such nano-columnar structures, a plan-view TEM image of the C-2 sample also has been conducted. The corresponding low magnification TEM image shows clear rows of NiO pillars. It is obvious that self-assembled NiO nanocolumnar (in dark contrast) with an average diameter of 5–10 nm are uniformly distributed in the BTO matrix (in bright contrast), as shown in Fig. 5(a) and (b). In the fast Fourier transformation (FFT) patterns transformed from the HRTEM image (Fig. 5(b)), the second order reflection of the (100) and (001) planes can be clearly observed. Double-diffraction spots are visible around each of these primary reflections. The double diffraction is a common feature for two-phase materials exhibiting epitaxial or topotaxial properties.[48] The films prepared with the growth mode of Fig. 1(c) have formed nanogranular structures. For G-1, the NiO nanoparticle are very fine (~2 nm in diameter and the spacing between them is about 5 nm) (Fig. S2†). As the ratio of NiO increases, the
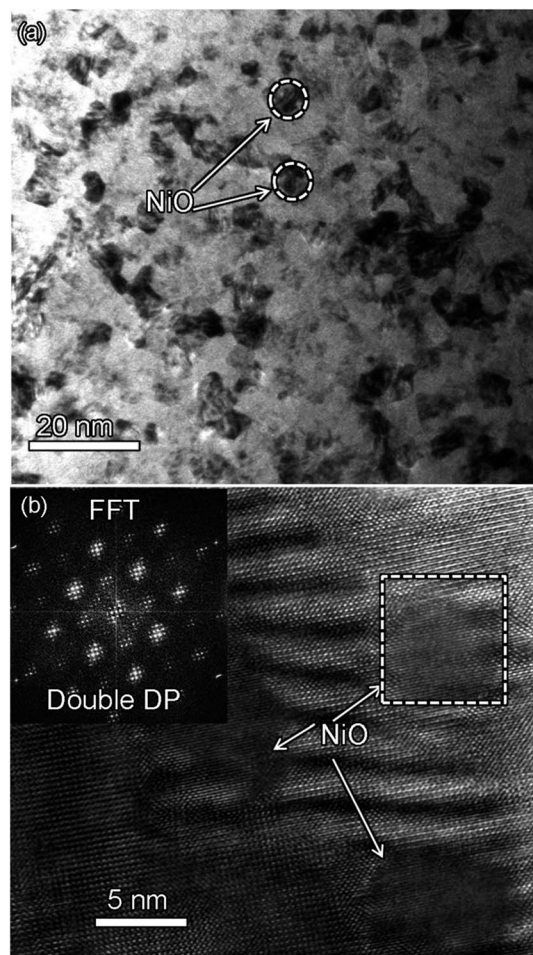
Fig. 5 (a) Plan-view TEM image of C-2 films with 20% NiO phase. It shows the NiO nanocolumnar in BTO matrix. (b) HRTEM image showing the vertical NiO nanocolumnar structure in BTO phase.

density of NiO nanoparticle increases and the diameter is about 5–10 nm (Fig. S3†). The results obtained in this study are in line with those of the nanogranular microstructures in $(Nd_{7/12}Li_{1/4})TiO_3$ reported by Guiton et al.[49] and in the decomposing deposited films of the $ZnMnGaO_4$ reported by Ni et al.[50] The XRD results and the corresponding HRTEM confirms the orientation relationships between BTO and NiO with the underlying STO substrate, i.e., $(001)_{BTO}//(002)_{NiO}//(001)_{STO}$ (out-of-plane) and $(100)_{BTO}//(200)_{NiO}//(100)_{STO}$ (in-plane). Based on the TEM results, typical depictions for the nanomultilayer, nanocolumnar, and nanogranular structure have been successfully prepared by tuning the growth mode, as shown in Fig. 1. The green part represents the BTO phase, while the pink part represents the NiO phase.

To further understand how the microstructures influence the functionalities of the composite films, the electric properties were investigated. Fig. 6(a) shows the FE polarization–electric field (P–E) hysteresis loops of the BTO:NiO nanomultilayer films with different NiO ratios. The switching frequency is 1 kHz and the maximum applied voltage is 20 V. From the well-defined P–E loops, we can rule out the extrinsic FE polarization. An interesting phenomenon is that the P–E

loops show a symmetric polarization switching behavior with a weaker imprint effect (the horizontal shift of the FE hysteresis loops). The imprint effect means the presence of the built-in-electric field in FE films. It is noted that in the BTO:NiO nanocomposite films, there are almost not a built-in electric field for the different microstructures, which is quite different from the previous reports that showed a large imprint in the FE super-lattices.[51,52] Fig. 6(a) shows that the polarization properties of multilayer are sensitive to the thickness of the NiO. Compared to the pure BTO thin films, the remanent polarization (P_r) of the M-1 samples reaches above 24 μC cm^{-2} which increased by almost 71% by the addition of the NiO ultra-thin layers. However, the loops of M-2 become very slim and tilted compared with the M-1 samples. There is no loop for the thicker NiO layer of the M-3 films. For the nanocolumnar structure, as shown in Fig. 6(b), it can be seen that the P_r and P_s remarkably increase with increasing the NiO ratio. The P_r value for the C-1 was 26 μC cm^{-2}. These values were found to be greatly enhanced in comparison with the value of 14 μC cm^{-2} for a single layer BTO films (Fig. 6(c)). In this study, the increase in the P_r for the nanocolumnar samples probably is attributed to the increase of the out-of-plane parameters. It is noted that the enhanced tetragonality for the BTO films gives rise to the higher polarization.[53] The nanocolumnar films have a large average out-of-plane lattice parameter due to the strain effect, which allows more room for Ti displacements. However, compared with the loop of BTO pure thin film, the shape of the hysteresis loop of the C-2 samples is asymmetric polarization switching behavior with a larger imprint effects, indicating a large leakage for the C-2 samples.

The nanomultilayer and nanocolumnar films can be explained within the framework of a resistance–capacitance (RC) model,[10,54] arising as a result of the well-ordered 3D geometric shapes and arrangements of the BTO and NiO phases in the composite films, as shown in Fig. 7. The green part represents the BTO phase, while the pink part represents the NiO phase. The enhancement in the remanent polarization for the M-1 samples is quite considerable. In generally, for the nanomultilayer films, the effect of electrostatic interaction plays the key role in determining the values of the P_r. The electrostatic interaction is related to the properties and the thickness of non-ferroelectric layer. NiO, having a very low electrical conductivity of less than 10^{-13} $(\Omega \text{ cm})^{-1}$ at room temperature, is a Mott–Hubbard insulator dielectric.[55,56] The theoretical predicted electric-field-breakdown of a Mott insulator dielectric is much larger than that of a band insulator dielectric.[57,58] For the M-1 with ultra-thin NiO layers, the insulating BTO matrix ferroelectric domains will switch as the electrical field can traverse the NiO layer due to the sufficiently thin insulator layer, as shown in Fig. 7(a). For the M-2 samples with thicker NiO layer, the energy cost of the polarizing NiO increase (or even not polarized due to the pure resistance properties of NiO) and the electric field displacement in the out-of-plane direction cannot be constant throughout the BTO:NiO nanocomposites, as shown in Fig. 7(b). However, compared with the loop of BTO pure thin film, the shape of the hysteresis loop of the C-2 samples is asymmetric polarization switching behavior with
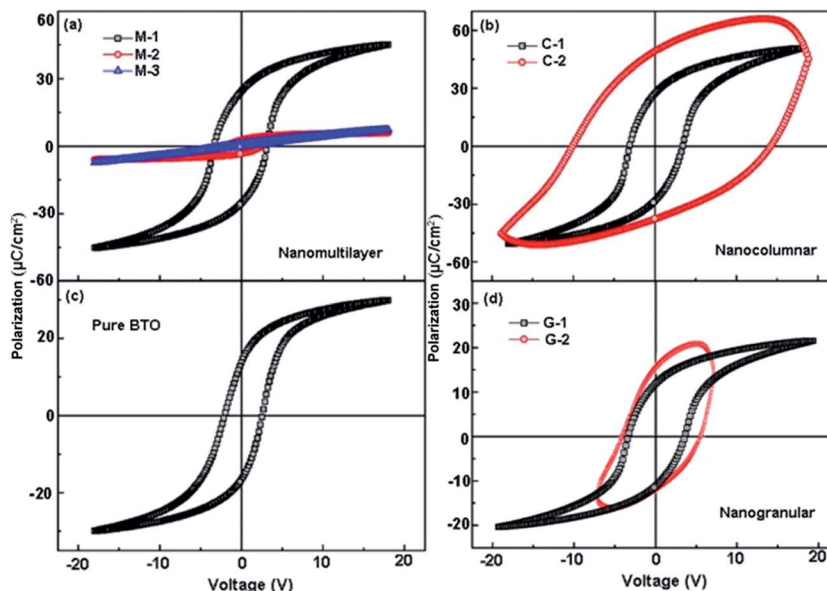
Fig. 6 (a and b) Polarization–voltage characteristics of the BTO:NiO nanocomposite films with the nanomultilayer and nanocolumnar structure (c) P–V characteristics of the pure BTO and BTO:NiO nanogranular structure measured at room temperatures at a frequency of 1 kHz. (d) Polarization–voltage characteristics of the BTO:NiO nanocomposite films with the nanogranular structure.
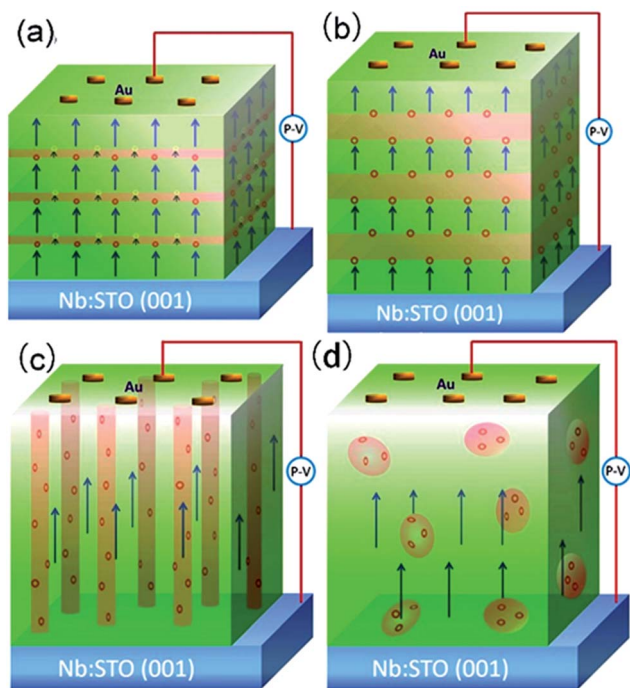

Fig. 7 Schematic diagram to show the large space charges concentration accumulated to the interface for the BTO:NiO and the movement of charges in an electric field. (a) Is the nanomultilayer with ultrathin NiO layers and (b) is the nanomultilayer with thicker NiO layers. (c) and (d) is the nanocolumnar and nanogranular structures, respectively. The green part represents the BTO phase, while the pink part represents the NiO phase. The red and yellow circles represent the space charges. The arrows represent the ferroelectric domains.

a larger imprint effects, indicating a large leakage for the C-2 samples. The electronically conductive channels in the BTO:-NiO nanocomposite films are the vertical interfaces of BTO and

NiO, as the bulk BTO and NiO parts are more electronically insulating compared with their vertical interfaces.[2] For the nanogranular structures, as shown in Fig. 6(d), the P_r value for the G-1 sample was 18 μC cm^{-2}. This value was slightly increased compared with the pure BTO films. However, G-2 samples do not show a well-defined saturated hysteresis loop, indicating a large leakage for these samples. The polarization decreased as the formation of polydomains due to the large particles of NiO.

Fig. 8 shows that the leakage current (J) as a function of voltage (V) of the BTO:NiO nanocomposite films and pure BTO films at room temperature. In the present study, all the leakage current measurements have been performed with a delay time of 80 ms to avoid polarization current.[59] It can be seen that the leakage current density of the nanomultilayer is the smallest among them, as shown in Fig. 8(a). The values of the leakage are of two orders of magnitude smaller than that of the pure BTO films. For the nanomultilayer structure, the J decreases with increasing the thickness of NiO layer. Fig. 8(b) shows that the values of the leakage nanocolumnar structure are comparable with the pure BTO film for the C-1. However, the leakage current density of 10^{-1} A cm^{-2} at ±100 kV cm^{-1} at room temperature has been observed in C-2 samples. Fig. 8(d) shows that the magnitude of leakage current density of the nanogranular thin film G-2 is approximately four orders larger than the pure films.

After I–V data acquisition, several conductive mechanisms have been proposed for the leakage current evolutions, such as Schottky emission (SE), Poole–Frenkel emission (PF), Fowler–Nordheim tunneling (FN), and space charge limited current (SCLC).[60–62] It has been well accepted that the conduction mechanisms in BTO:NiO nanocomposite films include two kinds: bulk limited (SCLC or PF) and interface limited (SE and FN). On the one hand, the J–E curves of the nanomultilayer films
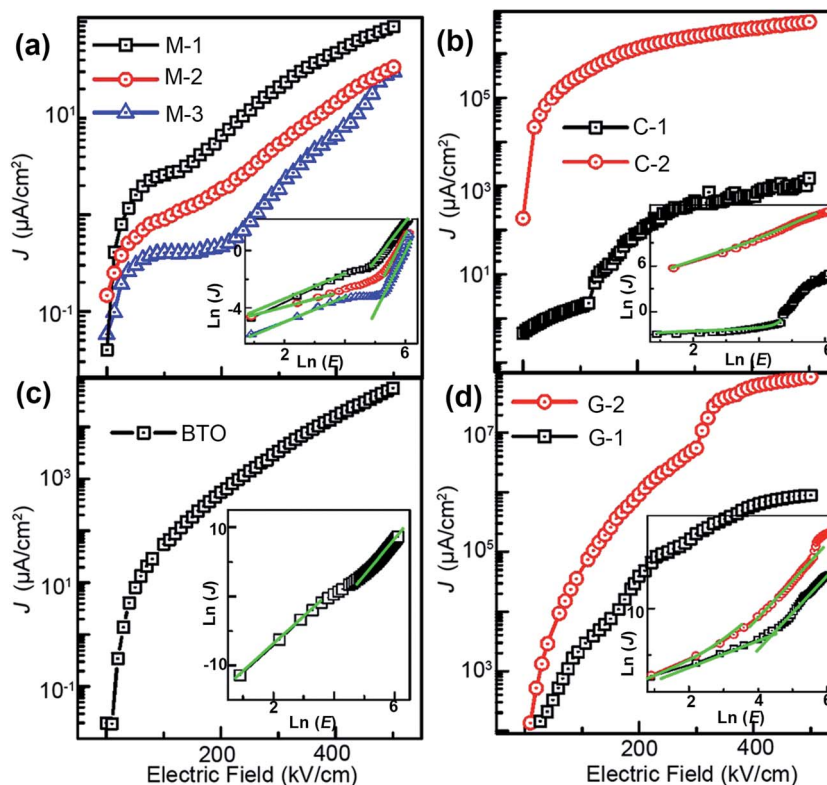
Fig. 8 (a–d) Leakage current density (J) as a function of the electric voltage (E) for the pure BTO film and BTO:NiO nanocomposite films. Inset: ln J versus ln E for pure BTO and BTO:NiO nanocomposite films at a positive bias (the values of the slope of the fitted lines are marked).

cannot be fitted well by the interface limited mechanism, indicating the bulk limited conduction mechanisms in these structures. Inset of Fig. 8(a) shows ln J–ln E curves at the positive bias for the nanomultilayer. At low electric fields, the slops of curves are close to 1, meaning that the leakage current in the nanomultilayer is accorded with Ohm's law. At high electric fields, it can be fitted quite well by the SCLC mechanism and described by Child's law:[63]

$$J \propto \frac{\mu \varepsilon_0 \varepsilon_r E^\alpha}{d} \qquad (1)$$

where μ is the charge carrier mobility, ε_0 is the permittivity of free space, ε_r is the relative dielectric constant, d is the film thickness, and α is a trap-dependent exponential factor. At high electric fields, the α for the M-1 are about 2.8, which is close to 2, indicating that the leakage current is accorded with the space charge limited conduction.[25] With increasing the thickness of NiO, the large slope values ($\alpha \approx 3.7$ for M-2, and $\alpha \approx 5.7$ for M-3) indicate that another conduction mechanism (PF) exists.[64] The magnitude of the leakage current in the nanomultilayer is mainly determined by the charge carrier mobility, which will be largely reduced due to the insulating behavior of ultrathin Mott-insulator of NiO layers. The strong electron–electron repulsion will prevent charge tunneling through NiO and hence reduce the charge leakage along the out-of-plane direction.[65,66] Therefore, it can be concluded that the insertion of NiO is also an effective way to reduce the leakage dramatically in the BTO based nanomultilayer, as shown in Fig. 8(a) and (b).

On the other hand, the J–E curves of the nanocolumnar films of C-1 and the nanogranular films can be fitted well by the modified Langmuir–Child law:[67,68]

$$J \propto aE + bE^2 \qquad (2)$$

here the coefficients a and b indicate the ohmic and space charge limited, respectively. It can be found that a decreases much faster than b for the nanocolumnar films of C-1 compared with the nanogranular films of G-1 and G-2. This indicates that the bulk-generated carriers are gradually exceeded by the injected electrons for the nanogranular films. However, for the nanocolumnar films of C-2, at low electric fields and the high electric fields, it can be fitted quite well by the SCLC mechanism and described by Child's law with the α for the C-2 are about 1.4–1.5. Due to the nanoculomnar structure, as shown in Fig. 7(c), the electronically conductive channels in the BTO:NiO nanocomposite films are parallel to the electric field, as the bulk BTO and NiO parts are more electronically insulating, and the SCLC is mainly confined by the vertical interface.

The dielectric properties are also strongly influenced by the presence of doping, grain boundaries, grain size, microstructure, and the concentration of charge carriers.[69] Therefore, study of the dielectric properties with different microstructures may help to better understand the intrinsic and extrinsic electrical properties of BTO:NiO nanocomposite. To investigate the effect of microstructure on the electrical properties of BTO:NiO
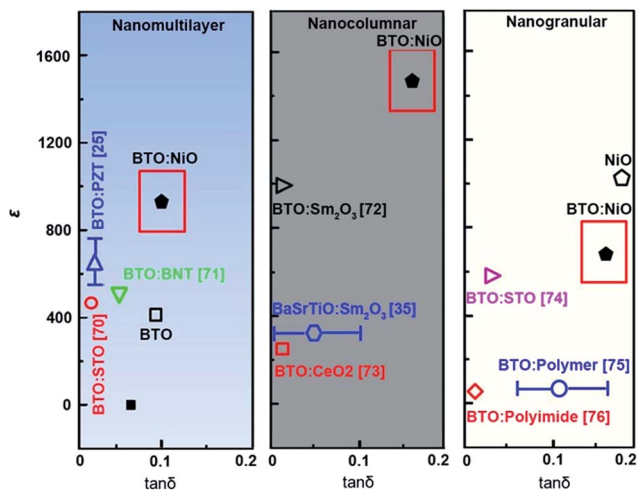
Fig. 9 ε versus tan δ for the pure BTO, NiO film and BTO:NiO nano-composite films with different microstructures measured at 10 kHz. Some data for epitaxial ferroelectric superlattices and composite films from the literatures are also shown.

nanocomposite films, we studied the dielectric properties of BTO:NiO nanocomposite films with the NiO ratio of 10% and 20% for the nanomultilayer (M-1 and M-2), nanocolumnar (C-1 and C-2) and nanogranular (G-1 and G-2) structure. The frequency dependence of dielectric constant has been measured at room temperature. Fig. 9 shows the representative frequency dependence of the real part, ε, of relative dielectric constant of BTO:NiO. From Fig. 9, it can be seen that the BTO:NiO nanocomposite films with different microstructures have high dielectric constants compared with other BTO based nanocomposite films, such as BTO:Sm$_2$O$_3$, BTO:polymer and BTO:STO composite films.[25,35,70–76]

For the BTO:NiO nanomultilayer, the dielectric constant is about 646 and 873 for the M-1 and M-2 samples, respectively, much larger than the pure films. The previous work has shown that the ε_{BTO} is about 200–400 for the BTO films with thickness of 100–200 nm.[77] Compared with the pure BTO and NiO films, the BTO:NiO nanomultilayers show a weak frequency dependence of the effective dielectric constant (ε_M) in the range from 10 kHz to 100 kHz. The lower dielectric loss in the BTO:NiO nanomultilayers at low frequency is consistent with their lower leakage current compared with the nano-columnar and nanogranular structure, which is due to the lower concentration of the mobile charged defects restricted by the BTO:NiO interfaces. To further describe the abnormal increase of the ε_M for the nanomultilayers, the films can be explained within the framework of a series connection of the BTO and NiO layers,[25] arising as a result of the well-ordered 3D geometric shapes and arrangements of the BTO and NiO phases in the composite films, as shown in Fig. 7(a). The ε_M can be expressed as:[78]

$$\varepsilon_M = \frac{t_{BTO} + t_{NiO}}{\dfrac{t_{BTO}}{\varepsilon_{BTO}} + \dfrac{t_{NiO}}{\varepsilon_{NiO}}} \quad (3)$$

where, t_{BTO} and ε_{BTO} are the thickness and relative dielectric constant of the BTO layer, and t_{NiO} and ε_{NiO} are the thickness and relative dielectric constant of the NiO layer. The calculated dielectric constant is shown in Fig. 10(a). The ε_M at 10 kHz for the BTO:NiO nanomultilayers are calculated by using the series model to be approximately 570. In contrast, the measured value of ε_M for the BTO:NiO nanomultilayers is 873. Compared to the uncoupled condition, the BTO:NiO nanomultilayers exhibits an enhancement of almost 60% in the dielectric constant. This means that the BTO:NiO interfaces play a very important role in the dielectric properties of the BTO:NiO nanomultilayers. In those previous works, the enhanced dielectric constants in the nanomultilayer were mainly considered for the Maxwell–Wagner effect and the space charges accumulated effects at the interface. The space charges accumulated at the BTO:NiO interfaces can reduce the pinning effect of defects on the motion of domain walls. Therefore, a low excitation field can easily make the motion of domain walls, and the dependence of dielectric constant on the electric field is relatively weak. These above results further confirmed that the BTO:NiO interfaces play a very important role for the enhanced electrical properties of the BTO:NiO nanomultilayer.

For the BTO:NiO nanocolumnar films, the dielectric constant is about 1083 and 1501 at 10 kHz for C-1 and C-2 samples, respectively. Fig. 10(b) shows that C-2 films exhibit an enhancement of almost 240% in the dielectric constant compared with the pure BTO films. Though the contribution of
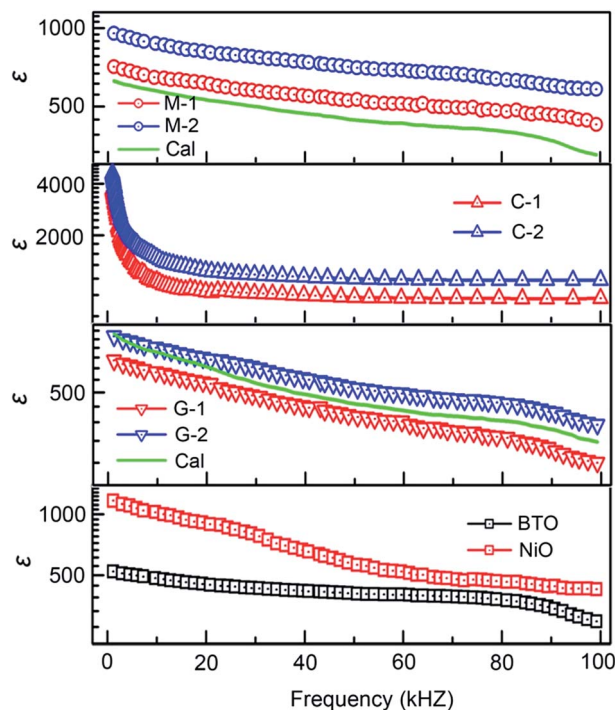

Fig. 10 Frequency dependence of the dielectric constants (ε) for the pure BTO, NiO film and the BTO:NiO nanocomposite films. The green line is the calculated data for the nanomultilayer and nanogranular structure with the series model and the Maxwell–Garnett theory, respectively.

the lateral interfaces may dominate the dielectric behavior in the nanomultilayer structures, the dielectric behavior of the BTO:NiO nanocolumnar films is totally different from those of the nanomultilayer thin films. The insulating BTO matrix exhibited ferroelectric domains, whereas the resistive NiO pillars exhibited pure dielectric properties. Compared with the nanomultilayer structure, the BTO:NiO nanocolumnar films show a strong frequency dependence of the effective dielectric constant (ε_C) in the range from 10 kHz to 100 kHz. On the one hand, as we discussed earlier, the not well ordered vertical nanopillar will introduce density of misfit dislocations. It is well known that dislocations have been demonstrated to be intrinsic defects and are often unavoidable in the nanocolumnar structure.[18] The ε_C value is large for the nanocolumnar structure at low frequencies, which is likely due to the charge accumulation at the interfaces. On the other hand, the ε_C decreased with increasing the frequency due to the high periodic reversal of the field at the interfaces. Consequently, the contribution of charge carriers to the dielectric constant was rapidly decreased.[79] However, the substantial increase in the permittivity of the BTO:NiO nanocolumnar films is very complex. On the other hand, Lee *et al.* found that enhanced tetragonality for the FE films gives rise to the higher permittivity.[24] In this work, the BTO:NiO nanocolumnar composite films have a large average out-of-plane lattice parameter due to the vertical strain effect, which allows more room for Ti displacements and therefore enhance the dielectric properties.

As shown in Fig. 10(c), the dielectric constant is about 594 and 650 for the G-1 and G-2 samples, respectively, much larger than the pure films. For the G-2 samples, the dielectric constant is increased by 30% with respect to the pure BTO films. Interestingly, the G-1 and G-2 samples show a weak frequency dependence of the effective dielectric constant (ε_G) in the range from 10 kHz to 100 kHz, in line with the nanomultilayer structures. Compared with the nanomultilayer and nanocolumnar structures, the lower dielectric constant in the nanogranular structure at low frequency is consistent with their higher leakage current, as shown in Fig. 8(d). The dielectric property of nanogranular composite films has been studied by previous researchers.[80,81] The insulating BTO matrix exhibited ferroelectric domains, whereas the resistive NiO nanoparticles (NPs) exhibited pure dielectric properties. It is noted that, the dielectric property could be effectively modified in the nanogranular structure by a proper addition of NiO nanoparticles, satisfying with the Maxwell–Garnett theory as follows:[82]

$$\varepsilon_G = \varepsilon_1 \frac{(\varepsilon_2 + \varepsilon_1) + 2p(\varepsilon_2 - \varepsilon_1)}{(\varepsilon_2 + \varepsilon_1) - p(\varepsilon_2 - \varepsilon_1)} \quad (4)$$

where ε_1 and ε_2 are the permittivity of the BTO matrix and the NiO, respectively, and p corresponds to the volume fraction of the NiO. Consequently, the effective permittivity increases with the increasing of NiO ratios. Interestingly, the calculated ε_C for the BTO:NiO nanogranular film is in line with the measured value. However, it must be noted that, due to poor crystal quality and the larger size of NiO NPs, many macroscopic domains begin to disappear and domain wall motion is limited by NiO NPs and defects. The dielectric losses of this composites jump

to high values, which counteract the benefits of the enhancement in the dielectric constants. Such a high dielectric loss can lead to a severe energy loss, which is undesirable for practical application.

Conclusions

In this study, epitaxial BTO:NiO nanocomposite films with different NiO fractions and microstructures have been grown on (001) Nb:STO substrates by PLD. For the composite films with a NiO ratio of 10% and 20%, the microstructures such as nanomultilayer, nanocolumnar and nanogranular have been successfully tuned by controlling the growth modes of the BTO and NiO. The values of polarization and dielectricity are sensitive to the microstructure. By tuning the microstructures, significantly enhanced polarization (24 $\mu C\ cm^{-2}$ for the nanomultilayer structures) and dielectric constant (873 and 1320 for the nanomultilayer and nanocolumnar structures, respectively) could be realized in these composite films. Our results show that the FE properties of BTO based nanocomposite films can be more effectively modulated by tuning their microstructures.

Acknowledgements

Notes and references

1 M. Fan, B. Zhang, H. Wang, J. Jian, X. Sun, J. J. Huang, L. G. Li, X. H. Zhang and H. Y. Wang, *Adv. Mater.*, 2017, **29**, 1606861.

2 S. Cho, C. Yun, S. Tappertzhofen, A. Kursumovic, S. Lee, P. Lu, Q. X. Jia, M. Fan, J. Jian, H. Y. Wang, S. Hofmann and J. L. MacManus-Driscoll, *Nat. Commun.*, 2016, **7**, 12373.

3 O. M. Hemeda, K. R. Mahmoud, T. Sharshar, M. Elsheshtawy and M. A. Hamad, *J. Magn. Magn. Mater.*, 2017, **429**, 124–128.

4 M. Zhuravlev, R. Sabirianov, S. Jaswal and E. Tsymbal, *Phys. Rev. Lett.*, 2005, **94**, 246802.

5 X. Q. Liu, J. Iocozzia, Y. Wang, X. Cui, Y. H. Chen, S. Q. Zhao, Z. Li and Z. Q. Lin, *Energy Environ. Sci.*, 2017, **10**, 402–434.

6 W. J. Ong, L. L. Tan, S. P. Chai, S. T. Yong and A. R. Mohamed, *ChemSusChem*, 2014, **7**, 690–719.

7 X. K. Ning, Z. J. Wang and Z. D. Zhang, *Adv. Mater. Interfaces*, 2015, **2**, 1500302.

8 A. Chen, J.-M. Hu, P. Lu, T. N. Yang, W. R. Zhang, L. G. Li, T. Ahmed, E. Enriquez, M. Weigand, Q. Su, H. Y. Wang, J.-X. Zhu, J. L. MacManus-Driscoll, L.-Q. Chen, D. Yarotski and Q. X. Jia, *Sci. Adv.*, 2016, **2**, e1600245.

9 H. M. Zheng, Q. Zhan, F. Zavaliche, M. Sherburne, F. Straub, M. P. Cruz, L. Q. Chen, U. Dahmen and R. Ramesh, *Nano Lett.*, 2006, **6**, 1401–1407.

10 X. K. Ning, Z. J. Wang and Z. D. Zhang, *Adv. Funct. Mater.*, 2014, **24**, 5393–5401.

11 M. Zhou, Y. L. Li, I. Jeon, Q. H. Yi, X. B. Zhu, X. W. Tang, H. Y. Wang, L. Fei, Y. P. Sun, S. G. Deng, Y. Matsuo, H. M. Luo and G. F. Zouc, *Sci. Rep.*, 2016, **6**, 26390.

12 S. Fusil, V. Garcia, A. Barthélémy and M. Bibes, *Annu. Rev. Mater. Res.*, 2014, **44**, 91.

13 T. Walther, R. Köferstein and S. G. Ebbinghaus, *J. Am. Ceram. Soc.*, 2017, **100**, 1502–1507.

14 H. L. Wang, X. K. Ning and Z. J. Wang, *RSC Adv.*, 2015, **5**, 76783–76787.

15 X. K. Ning, Microstructure of the Nanostructured Oxide Composite Thin Films and Its Functional Properties, *Outlook and Challenges of Nano Devices, Sensors, and MEMS*, Springer International Publishing, 2017, pp. 397–427.

16 P. Zubko, N. Jecklin, A. Torres-Pardo, P. Aguado-Puente, A. Gloter, C. Lichtensteiger, J. Junquera, O. Steìphan and J.-M. Triscone, *Nano Lett.*, 2012, **12**, 2846–2851.

17 M. Dawber, N. Stucki, C. Lichtensteiger, S. Gariglio, P. Ghosez and J. Triscone, *Adv. Mater.*, 2007, **19**, 4153–4159.

18 W. W. Li, W. Zhang, L. Wang, J. X. Gu, A. P. Chen, R. Zhao, Y. Liang, H. Z. Guo, R. J. Tang, C. C. Wang, K. J. Jin, H. Y. Wang and H. Yang, *Sci. Rep.*, 2015, **5**, 11335.

19 H. Huang, *Nat. Photonics*, 2010, **4**, 134–135.

20 V. Garcia, S. Fusil, K. Bouzehouane, S. Enouz-Vedrenne, N. D. Mathur, A. Barthélémy and M. Bibes, *Nature*, 2009, **460**, 81.

21 M. Dawber and E. Bousquet, *MRS Bull.*, 2013, **38**, 1048–1055.

22 E. Bousquet, M. Dawber, N. Stucki, C. Lichtensteiger, P. Hermet, S. Gariglio, J.-M. Triscone and P. Ghosez, *Nature*, 2008, **452**, 732–736.

23 H. Tabata, H. Tanaka and T. Kawai, *Appl. Phys. Lett.*, 1994, **65**, 1970–1972.

24 H. N. Lee, H. M. Christen, M. F. Chisholm, C. M. Rouleau and D. H. Lowndes, *Nature*, 2005, **433**, 395–399.

25 B. He and Z. J. Wang, *ACS Appl. Mater. Interfaces*, 2016, **8**, 6736–6742.

26 J. J. Peng, C. Song, B. Cui, F. Li, H. J. Mao, G. Y. Wang and F. Pan, *Appl. Phys. Lett.*, 2015, **107**, 182904.

27 Y. Liu, Y. L. Zhu, Y. L. Tang, Y. J. Wang, Y. X. Jiang, Y. B. Xu, B. Zhang and X. L. Ma, *Nano Lett.*, 2017, **17**, 3619.

28 F. F. Ge, L. Bai, W. D. Wu, L. H. Cao, X. M. Wang, Y. J. Ma, S. J. Han, H. P. Wang, X. Y. An, H. B. Wang and J. Shen, *J. Cryst. Growth*, 2015, **312**, 2489–2493.

29 F. F. Ge, X. M. Wang, L. H. Cao, J. Li, H. L. Zhang, H. P. Wang, Y. Bai, H. B. Wang, J. Shen and W. D. Wu, *Nanoscale Res. Lett.*, 2010, **5**, 834–838.

30 Z. R. Wang, T. Hu, L. W. Tang, M. Ning, C. L. Song, G. R. Han, W. J. Weng and P. Y. Du, *Appl. Phys. Lett.*, 2008, **93**, 222901–222904.

31 W. D. Wu, Y. J. He, F. Wang, Z. H. Chen, Y. J. Tang and W. G. Sun, *J. Cryst. Growth*, 2006, **289**, 408–413.

32 Y. J. Wu, H. L. Wang, X. K. Ning, Z. J. Wang and Q. Wang, *J. Inorg. Mater.*, 2015, **30**, 207–213.

33 A. Cazacu, L. Curecheriu, A. Neagu, L. Padurariu, A. Cernescu, I. Lisiecki and L. Mitoseriu, *Appl. Phys. Lett.*, 2013, **102**, 222903.

34 H. Zheng, J. Wang, S. E. Lofland, Z. Ma, L. Mohaddes-Ardabili, T. Zhao, L. Salamanca-Riba, S. R. Shinde, S. B. Ogale, F. Bai, D. Viehland, Y. Jia, D. G. Schlom, M. Wuttig, A. Roytburd and R. Ramesh, *Science*, 2004, **303**, 661.

35 O. J. Lee, S. A. Harrington, A. Kursumovic, E. Defay, H. Y. Wang, Z. X. Bi, C.-F. Tsai, L. Yan, Q. X. Jia and J. L. MacManus-Driscoll, *Nano Lett.*, 2012, **12**, 4311–4317.

36 R. Zhao, W. W. Li, J. H. Lee, E. M. Choi, Y. Liang, W. Zhang, R. J. Tang, H. Y. Wang, Q. X. Jia, J. L. MacManus-Driscoll and H. Yang, *Adv. Funct. Mater.*, 2014, **24**, 5240–5245.

37 P. Lunkenheimer, A. Loidl, C. R. Ottermann and K. Bange, *Phys. Rev. B: Condens. Matter Mater. Phys.*, 1991, **44**, 5927.

38 J. B. Wu, C. W. Nan, Y. H. Lin and Y. Deng, *Phys. Rev. Lett.*, 2002, **89**, 271601.

39 C. Pecharromán, F. Esteban-Betegón, J. F. Bartolomé, S. López-Esteban and J. S. Moya, *Adv. Mater.*, 2001, **13**, 1541–1544.

40 M. Saleem, I. S. Kim, J. S. Song, S. J. Jeong, M. S. Kim and S. Yoon, *Ceram. Int.*, 2014, **40**, 7329–7335.

41 S. J. Callori, J. Gabel, D. Su, J. Sinsheimer, M. V. Fernandez-Serra and M. Dawber, *Phys. Rev. Lett.*, 2012, **109**, 067160.

42 L. X. Li, R. X. Fu, Q. W. Liao and L. J. Ji, *Ceram. Int.*, 2012, **38**, 1915.

43 J. Q. Huang, P. Y. Du, W. J. Weng and G. R. Han, *J. Electroceram.*, 2008, **21**, 394.

44 S. Li, X. H. Wei, Y. Lei, X. C. Yuan and H. Z. Zeng, *Appl. Surf. Sci.*, 2016, **389**, 977.

45 D. Nuzhnyy, J. Petzelt, V. Bovtun, T. Ostapchuk, M. Savinov, M. Kempa, P. Bednyakov, L. Fernández-Garciá, T. Rodriguez-Suarez and J. L. Menendéz, *Ferroelectrics*, 2016, **500**, 1.

46 F. C. Frank and J. H. van der Merwe, *Proc. R. Soc. London, Ser. A*, 1949, **198**, 205.

47 S. L. Yuan, Y. P. Yang, Z. C. Xia, G. Peng, G. H. Zhang, J. Tang, J. Liu, L. J. Zhang, Q. H. Zhong, S. Liu, L. Chen, W. Feng, Z. Y. Li, L. Liu, G. Q. Zhang, F. Tu and C. S. Xiong, *Solid State Commun.*, 2002, **123**, 55.

48 D. B. Williams and C. B. Carter, *Transmission Electron Microscopy: A Textbook for Materials Science*, Plenum, New York, 1996.

49 B. S. Guiton, H. Wu and P. K. Davies, *Chem. Mater.*, 2009, **20**, 2860.

50 Y. Ni, W. F. Rao and A. G. Khachaturyan, *Nano Lett.*, 2009, **9**, 3275.

51 N. Ortega, A. Kumar, O. A. Maslova, Y. I. Yuzyuk, J. F. Scott and R. S. Katiyar, *Phys. Rev. B: Condens. Matter Mater. Phys.*, 2011, **83**, 144108.

52 K. Boldyreva, L. Pintilie, A. Lotnyk, I. B. Misirlioglu, M. Alexe and D. Hesse, *Appl. Phys. Lett.*, 2007, **91**, 122915.

53 K. J. Choi, M. Biegalski, Y. L. Li, A. Sharan, J. Schubert, R. Uecker, P. Reiche, Y. B. Chen, X. Q. Pan, V. Gopalan, L.-Q. Chen, D. G. Schlom and C. B. Eom, *Science*, 2004, **306**, 1005–1009.

54 S. A. Fedoseev, A. V. Pan, S. Rubanov, I. A. Golovchanskiy and O. V. Shcherbakova, *ACS Nano*, 2013, **7**, 286.

55 K. Terakura, A. R. Williams, T. Oguchi and J. Kubler, *Phys. Rev. Lett.*, 1984, **52**, 1830.

56 J. M. Mckay and V. E. Henrich, *Phys. Rev. Lett.*, 1984, **53**, 2343.

57 D. Puggioni, G. Giovannetti, M. Capone and J. M. Rondinelli, *Phys. Rev. Lett.*, 2015, **115**, 087202.

58 H. Gomi, T. J. Inagaki and A. Takahashi, *Phys. Rev. B*, 2016, **93**, 035105.

59 C. Bhardwaj and D. Kaur, *J. Alloys Compd.*, 2014, **595**, 158.

60 I. Boerasu, L. Pintilie, M. Pereira, M. I. Vasilevskiy and M. J. M. Gomes, *J. Appl. Phys.*, 2003, **93**, 4776.

61 M. T. Chentir, E. Bouyssou, L. Ventura and C. Anceau, *J. Appl. Phys.*, 2009, **105**, 061605.

62 D. Lee, S. H. Baek, T. H. Kim, J.-G. Yoon, C. M. Folkman, C. B. Eom and T. W. Noh, *Phys. Rev. B: Condens. Matter Mater. Phys.*, 2011, **84**, 125305.

63 W. Li, R. Zhao, R. Tang, A. Chen, W. Zhang, X. Lu, H. Wang and H. Yang, *ACS Appl. Mater. Interfaces*, 2014, **6**, 5356–5361.

64 R. Barman and D. Kaur, *J. Alloys Compd.*, 2015, **644**, 506–512.

65 N. Mott, *J. Solid State Chem.*, 1990, **88**, 5.

66 M. Imada, A. Fujimori and Y. Tokura, *Rev. Mod. Phys.*, 1998, **70**, 1039.

67 X. Qi, J. Dho, R. Tomov, M. G. Blamire and J. L. MacManus-Driscoll, *Appl. Phys. Lett.*, 2005, **86**, 062903.

68 Z. Wen, X. Shen, J. X. Wu, D. Wu, A. D. Li, B. Yang, Z. Wang, H. Z. Chen and J. L. Wang, *Appl. Phys. Lett.*, 2010, **96**, 202904.

69 N. H. Vasoya, V. K. Lakhani, P. U. Sharma, K. B. Modi, R. Kumar and H. H. Joshi, *J. Phys.: Condens. Matter*, 2006, **18**, 8063–8092.

70 H.-N. Tsai, Y.-C. Liang and H.-Y. Lee, *J. Cryst. Growth*, 2005, **284**, 65–72.

71 M. Bousquet, L. Batista, J. L. Dellis, A. Boulle, U. Rabe, O. Durand-Drouhin, Y. Gagou, L. Dupont, V. Viallet, A. Zeinert, S. Hirsekorn and N. Lemée, *J. Appl. Phys.*, 2014, **116**, 194104.

72 S. A. Harrington, J. Y. Zhai, S. Denev, V. Gopalan, H. Y. Wang, Z. X. Bi, S. A. T. Redfern, S. H. Baek, C. W. Bark, C. B. Eom, Q. X. Jia, M. E. Vickers and J. L. MacManus-Driscoll, *Nat. Nanotechnol.*, 2011, **6**, 491–495.

73 F. Khatkhatay, A. Chen, J. H. Lee, W. Zhang, H. Abdel-Raziq and H. Wang, *ACS Appl. Mater. Interfaces*, 2013, **5**, 12541–12547.

74 N. Suzuki, M. B. Zakaria, N. L. Torad, K. C.-W. Wu, Y. Nemoto, M. Imura, M. Osada and Y. Yamauchi, *Chem.–Eur. J.*, 2013, **19**, 4446–4450.

75 R. Popielarz, C. K. Chiang, R. Nozaki and J. Obrzut, *Macromolecules*, 2001, **34**, 5910–5915.

76 S. F. Wang, Y. R. Wang, K. C. Cheng and Y. P. Hsaio, *Ceram. Int.*, 2009, **35**, 265–268.

77 B. H. Hoerman, G. M. Ford, L. D. Kaufmann and B. W. Wessels, *Appl. Phys. Lett.*, 1998, **73**, 2248.

78 A. K. Tagantsev, V. O. Sherman, K. F. Astafiev, J. Venkatesh and N. Setter, *J. Electroceram.*, 2003, **11**, 5–66.

79 L. J. Chen, L. P. Li and G. S. Li, *J. Solid State Chem.*, 2008, **181**, 2073–2077.

80 Z. Wang, T. Hu, L. Tang, N. Ma, C. Song, G. Han, W. Weng and P. Du, *Appl. Phys. Lett.*, 2008, **93**, 222901.

81 N. Tsutsumi, R. Kosugi, K. Kinashi and W. Sakai, *ACS Appl. Mater. Interfaces*, 2016, **8**, 16816–16822.

82 T. Liu, Y. Pang, M. Zhu and S. Kobayashi, *Nanoscale*, 2014, **6**, 2447–2454.